Biomedical Optics EXPRESS

Imaging deep skeletal muscle structure using a high-sensitivity ultrathin side-viewing optical coherence tomography needle probe

Xiaojie Yang,[1,*] Dirk Lorenser,[1] Robert A. McLaughlin,[1] Rodney W. Kirk,[1] Matthew Edmond,[2] M. Cather Simpson,[2] Miranda D. Grounds,[3] and David D. Sampson[1,4]

[1]*Optical + Biomedical Engineering Laboratory, School of Electrical, Electronic, and Computer Engineering, The University of Western Australia, Crawley, Australia*
[2]*Photon Factory, School of Chemical Sciences & Department of Physics, University of Auckland, Auckland, New Zealand*
[3]*School of Anatomy, Physiology, and Human Biology, The University of Western Australia*
[4]*Centre for Microscopy, Characterisation and Analysis, The University of Western Australia, Crawley, Australia*
[*]*yangx06@student.uwa.edu.au*

Abstract: We have developed an extremely miniaturized optical coherence tomography (OCT) needle probe (outer diameter 310 μm) with high sensitivity (108 dB) to enable minimally invasive imaging of cellular structure deep within skeletal muscle. Three-dimensional volumetric images were acquired from *ex vivo* mouse tissue, examining both healthy and pathological dystrophic muscle. Individual myofibers were visualized as striations in the images. Degradation of cellular structure in necrotic regions was seen as a loss of these striations. Tendon and connective tissue were also visualized. The observed structures were validated against co-registered hematoxylin and eosin (H&E) histology sections. These images of internal cellular structure of skeletal muscle acquired with an OCT needle probe demonstrate the potential of this technique to visualize structure at the microscopic level deep in biological tissue *in situ*.

OCIS codes: (060.2370) Fiber optics sensors; (170.4500) Optical coherence tomography; (170.6935) Tissue characterization; (230.3990) Micro-optical devices.

References and links

1. E. N. Marieb, "Human anatomy & physiology," in *Human anatomy & Physiology*, K. Ueno, ed. (Daryl Fox, San Francisco, USA, 2001), p. 324.
2. K. Bushby, R. Finkel, D. J. Birnkrant, L. E. Case, P. R. Clemens, L. Cripe, A. Kaul, K. Kinnett, C. McDonald, S. Pandya, J. Poysky, F. Shapiro, J. Tomezsko, C. Constantin, and DMD Care Considerations Working Group, "Diagnosis and management of Duchenne muscular dystrophy, part 1: diagnosis, and pharmacological and psychosocial management," Lancet Neurol. **9**(1), 77–93 (2010).
3. E. P. Hoffman, K. H. Fischbeck, R. H. Brown, M. Johnson, R. Medori, J. D. Loire, J. B. Harris, R. Waterston, M. Brooke, L. Specht, W. Kupsky, J. Chamberlain, C. T. Caskey, F. Shapiro, and L. M. Kunkel, "Characterization of dystrophin in muscle-biopsy specimens from patients with Duchenne's or Becker's muscular dystrophy," N. Engl. J. Med. **318**(21), 1363–1368 (1988).
4. M. D. Grounds, H. G. Radley, G. S. Lynch, K. Nagaraju, and A. De Luca, "Towards developing standard operating procedures for pre-clinical testing in the *mdx* mouse model of Duchenne muscular dystrophy," Neurobiol. Dis. **31**(1), 1–19 (2008).
5. F. S. Foster, C. J. Pavlin, K. A. Harasiewicz, D. A. Christopher, and D. H. Turnbull, "Advances in ultrasound biomicroscopy," Ultrasound Med. Biol. **26**(1), 1–27 (2000).
6. S. Sipilä and H. Suominen, "Ultrasound imaging of the quadriceps muscle in elderly athletes and untrained men," Muscle Nerve **14**(6), 527–533 (1991).
7. K. D. Wallace, J. N. Marsh, S. L. Baldwin, A. M. Connolly, R. Keeling, G. M. Lanza, S. A. Wickline, and M. S. Hughes, "Sensitive ultrasonic delineation of steroid treatment in living dystrophic mice with energy-based and entropy-based radio frequency signal processing," IEEE Trans. Ultrason. Ferroelectr. Freq. Control **54**(11), 2291–2299 (2007).
8. J. Philpot, C. Sewry, J. Pennock, and V. Dubowitz, "Clinical phenotype in congenital muscular dystrophy: correlation with expression of merosin in skeletal muscle," Neuromuscul. Disord. **5**(4), 301–305 (1995).

#198712 - $15.00 USD Received 2 Oct 2013; revised 22 Nov 2013; accepted 30 Nov 2013; published 10 Dec 2013

9. J. Phoenix, D. Betal, N. Roberts, T. R. Helliwell, and R. H. T. Edwards, "Objective quantification of muscle and fat in human dystrophic muscle by magnetic resonance image analysis," Muscle Nerve **19**(3), 302–310 (1996).
10. M. Kobayashi, A. Nakamura, D. Hasegawa, M. Fujita, H. Orima, and S. Takeda, "Evaluation of dystrophic dog pathology by fat-suppressed T2-weighted imaging," Muscle Nerve **40**(5), 815–826 (2009).
11. J. N. Kornegay, J. A. Li, J. R. Bogan, D. J. Bogan, C. L. Chen, H. Zheng, B. Wang, C. P. Qiao, J. F. Howard, Jr., and X. A. Xiao, "Widespread muscle expression of an AAV9 human mini-dystrophin vector after intravenous injection in neonatal dystrophin-deficient dogs," Mol. Ther. **18**(8), 1501–1508 (2010).
12. H. Amthor, T. Egelhof, I. McKinnell, M. E. Ladd, I. Janssen, J. Weber, H. Sinn, H. H. Schrenk, M. Forsting, T. Voit, and V. Straub, "Albumin targeting of damaged muscle fibres in the *mdx* mouse can be monitored by MRI," Neuromuscul. Disord. **14**(12), 791–796 (2004).
13. L. M. McIntosh, R. E. Baker, and J. E. Anderson, "Magnetic resonance imaging of regenerating and dystrophic mouse muscle," Biochem. Cell Biol. **76**(2-3), 532–541 (1998).
14. V. Straub, K. M. Donahue, V. Allamand, R. L. Davisson, Y. R. Kim, and K. P. Campbell, "Contrast agent-enhanced magnetic resonance imaging of skeletal muscle damage in animal models of muscular dystrophy," Magn. Reson. Med. **44**(4), 655–659 (2000).
15. G. Walter, L. Cordier, D. Bloy, and H. L. Sweeney, "Noninvasive monitoring of gene correction in dystrophic muscle," Magn. Reson. Med. **54**(6), 1369–1376 (2005).
16. M. Swash, M. M. Brown, and C. Thakkar, "CT muscle imaging and the clinical assessment of neuromuscular disease," Muscle Nerve **18**(7), 708–714 (1995).
17. S. J. Schambach, S. Bag, V. Steil, C. Isaza, L. Schilling, C. Groden, and M. A. Brockmann, "Ultrafast high-resolution *in vivo* volume-CTA of mice cerebral vessels," Stroke **40**(4), 1444–1450 (2009).
18. X. Y. Zhu, M. Rodriguez-Porcel, M. D. Bentley, A. R. Chade, V. Sica, C. Napoli, N. Caplice, E. L. Ritman, A. Lerman, and L. O. Lerman, "Antioxidant intervention attenuates myocardial neovascularization in hypercholesterolemia," Circulation **109**(17), 2109–2115 (2004).
19. M. Ni, M. Zhang, S. F. Ding, W. Q. Chen, and Y. Zhang, "Micro-ultrasound imaging assessment of carotid plaque characteristics in apolipoprotein-E knockout mice," Atherosclerosis **197**(1), 64–71 (2008).
20. A. R. Patel, E. S. Y. Chan, D. E. Hansel, C. T. Powell, W. D. Heston, and W. A. Larchian, "Transabdominal micro-ultrasound imaging of bladder cancer in a mouse model: a validation study," Urology **75**(4), 799–804 (2010).
21. P. J. Bolan, E. Yacoub, M. Garwood, K. Ugurbil, and N. Harel, "*In vivo* micro-MRI of intracortical neurovasculature," Neuroimage **32**(1), 62–69 (2006).
22. S. J. Schambach, S. Bag, L. Schilling, C. Groden, and M. A. Brockmann, "Application of micro-CT in small animal imaging," Methods **50**(1), 2–13 (2010).
23. T. Masuda, N. Fujimaki, E. Ozawa, and H. Ishikawa, "Confocal laser microscopy of dystrophin localization in guinea pig skeletal muscle fibers," J. Cell Biol. **119**(3), 543–548 (1992).
24. M. Bartoli, N. Bourg, D. Stockholm, F. Raynaud, A. Delevacque, Y. Han, P. Borel, K. Seddik, N. Armande, and I. Richard, "A mouse model for monitoring calpain activity under physiological and pathological conditions," J. Biol. Chem. **281**(51), 39672–39680 (2006).
25. S. V. Plotnikov, A. M. Kenny, S. J. Walsh, B. Zubrowski, C. Joseph, V. L. Scranton, G. A. Kuchel, D. Dauser, M. S. Xu, C. C. Pilbeam, D. J. Adams, R. P. Dougherty, P. J. Campagnola, and W. A. Mohler, "Measurement of muscle disease by quantitative second-harmonic generation imaging," J. Biomed. Opt. **13**(4), 044018 (2008).
26. O. Friedrich, M. Both, C. Weber, S. Schürmann, M. D. H. Teichmann, F. von Wegner, R. H. A. Fink, M. Vogel, J. S. Chamberlain, and C. Garbe, "Microarchitecture is severely compromised but motor protein function is preserved in dystrophic *mdx* skeletal muscle," Biophys. J. **98**(4), 606–616 (2010).
27. R. S. Pillai, D. Lorenser, and D. D. Sampson, "Deep-tissue access with confocal fluorescence microendoscopy through hypodermic needles," Opt. Express **19**(8), 7213–7221 (2011).
28. M. E. Llewellyn, R. P. J. Barretto, S. L. Delp, and M. J. Schnitzer, "Minimally invasive high-speed imaging of sarcomere contractile dynamics in mice and humans," Nature **454**(7205), 784–788 (2008).
29. D. Huang, E. A. Swanson, C. P. Lin, J. S. Schuman, W. G. Stinson, W. Chang, M. R. Hee, T. Flotte, K. Gregory, C. A. Puliafito, and J. G. Fujimoto, "Optical coherence tomography," Science **254**(5035), 1178–1181 (1991).
30. B. R. Klyen, J. J. Armstrong, S. G. Adie, H. G. Radley, M. D. Grounds, and D. D. Sampson, "Three-dimensional optical coherence tomography of whole-muscle autografts as a precursor to morphological assessment of muscular dystrophy in mice," J. Biomed. Opt. **13**(1), 011003 (2008).
31. B. R. Klyen, T. Shavlakadze, H. G. Radley-Crabb, M. D. Grounds, and D. D. Sampson, "Identification of muscle necrosis in the *mdx* mouse model of Duchenne muscular dystrophy using three-dimensional optical coherence tomography," J. Biomed. Opt. **16**(7), 076013 (2011).
32. R. M. Lovering, S. B. Shah, S. J. P. Pratt, W. Gong, and Y. Chen, "Architecture of healthy and dystrophic muscles detected by optical coherence tomography," Muscle Nerve **47**(4), 588–590 (2013).
33. X. D. Li, C. Chudoba, T. Ko, C. Pitris, and J. G. Fujimoto, "Imaging needle for optical coherence tomography," Opt. Lett. **25**(20), 1520–1522 (2000).
34. Y. C. Wu, J. F. Xi, L. Huo, J. Padvorac, E. J. Shin, S. A. Giday, A. M. Lennon, M. I. F. Canto, J. H. Hwang, and X. D. Li, "Robust high-resolution fine OCT needle for side-viewing interstitial tissue imaging," IEEE J. Sel. Top. Quantum Electron. **16**(4), 863–869 (2010).
35. B. C. Quirk, R. A. McLaughlin, A. Curatolo, R. W. Kirk, P. B. Noble, and D. D. Sampson, "*In situ* imaging of lung alveoli with an optical coherence tomography needle probe," J. Biomed. Opt. **16**(3), 036009 (2011).
36. D. Lorenser, X. Yang, R. W. Kirk, B. C. Quirk, R. A. McLaughlin, and D. D. Sampson, "Ultrathin side-viewing needle probe for optical coherence tomography," Opt. Lett. **36**(19), 3894–3896 (2011).

#198712 - $15.00 USD Received 2 Oct 2013; revised 22 Nov 2013; accepted 30 Nov 2013; published 10 Dec 2013

37. R. A. McLaughlin, B. C. Quirk, A. Curatolo, R. W. Kirk, L. Scolaro, D. Lorenser, P. D. Robbins, B. A. Wood, C. M. Saunders, and D. D. Sampson, "Imaging of breast cancer with optical coherence tomography needle probes: feasibility and initial results," IEEE J. Sel. Top. Quantum Electron. **18**(3), 1184–1191 (2012).
38. R. A. McLaughlin, X. Yang, B. C. Quirk, D. Lorenser, R. W. Kirk, P. B. Noble, and D. D. Sampson, "Static and dynamic imaging of alveoli using optical coherence tomography needle probes," J. Appl. Physiol. **113**(6), 967–974 (2012).
39. L. Scolaro, D. Lorenser, R. A. McLaughlin, B. C. Quirk, R. W. Kirk, and D. D. Sampson, "High-sensitivity anastigmatic imaging needle for optical coherence tomography," Opt. Lett. **37**(24), 5247–5249 (2012).
40. R. A. McLaughlin, D. Lorenser, and D. D. Sampson, "Needle probes in optical coherence tomography," in *Handbook of Coherent-Domain Optical Methods: Biomedical Diagnostics, Environmental Monitoring, and Material Science*, V. V. Tuchin, ed. (Springer Science + Business, New York, USA, 2013), pp. 1065–1102.
41. V. X. D. Yang, Y. X. Mao, N. Munce, B. Standish, W. Kucharczyk, N. E. Marcon, B. C. Wilson, and I. A. Vitkin, "Interstitial Doppler optical coherence tomography," Opt. Lett. **30**(14), 1791–1793 (2005).
42. K. M. Tan, M. Shishkov, A. Chee, M. B. Applegate, B. E. Bouma, and M. J. Suter, "Flexible transbronchial optical frequency domain imaging smart needle for biopsy guidance," Biomed. Opt. Express **3**(8), 1947–1954 (2012).
43. W. A. Reed, M. F. Yan, and M. J. Schnitzer, "Gradient-index fiber-optic microprobes for minimally invasive *in vivo* low-coherence interferometry," Opt. Lett. **27**(20), 1794–1796 (2002).
44. B. A. Standish, K. K. C. Lee, X. Jin, A. Mariampillai, N. R. Munce, M. F. G. Wood, B. C. Wilson, I. A. Vitkin, and V. X. D. Yang, "Interstitial Doppler optical coherence tomography as a local tumor necrosis predictor in photodynamic therapy of prostatic carcinoma: an *in vivo* study," Cancer Res. **68**(23), 9987–9995 (2008).
45. M. S. Jafri, R. Tang, and C. M. Tang, "Optical coherence tomography guided neurosurgical procedures in small rodents," J. Neurosci. Methods **176**(2), 85–95 (2009).
46. A. E. Siegman, *Lasers* (University Science Books, CA, USA, 1986).
47. R. H. Colby, "Intrinsic birefringence of glycerinated myofibrils," J. Cell Biol. **51**(3), 763–771 (1971).
48. Y. Yeh, R. J. Baskin, R. A. Brown, and K. Burton, "Depolarization spectrum of diffracted light from muscle fiber. The intrinsic anisotropy component," Biophys. J. **47**(5), 739–742 (1985).
49. R. C. Haskell, F. D. Carlson, and P. S. Blank, "Form birefringence of muscle," Biophys. J. **56**(2), 401–413 (1989).
50. J. J. Pasquesi, S. C. Schlachter, M. D. Boppart, E. Chaney, S. J. Kaufman, and S. A. Boppart, "*In vivo* detection of exercised-induced ultrastructural changes in genetically-altered murine skeletal muscle using polarization-sensitive optical coherence tomography," Opt. Express **14**(4), 1547–1556 (2006).
51. X. Yang, L. Chin, B. R. Klyen, T. Shavlakadze, R. A. McLaughlin, M. D. Grounds, and D. D. Sampson, "Quantitative assessment of muscle damage in the *mdx* mouse model of Duchenne muscular dystrophy using polarization-sensitive optical coherence tomography," J. Appl. Physiol. **115**(9), 1393–1401 (2013).
52. A. Curatolo, R. A. McLaughlin, B. C. Quirk, R. W. Kirk, A. G. Bourke, B. A. Wood, P. D. Robbins, C. M. Saunders, and D. D. Sampson, "Ultrasound-guided optical coherence tomography needle probe for the assessment of breast cancer tumor margins," Am. J. Roentgenol. **199**(4), W520–W522 (2012).
53. J. M. Schmitt, A. Knüttel, M. Yadlowsky, and M. A. Eckhaus, "Optical-coherence tomography of a dense tissue: Statistics of attenuation and backscattering," Phys. Med. Biol. **39**(10), 1705–1720 (1994).
54. A. W. Sainter, T. A. King, and M. R. Dickinson, "Effect of target biological tissue and choice of light source on penetration depth and resolution in optical coherence tomography," J. Biomed. Opt. **9**(1), 193–199 (2004).
55. L. Scolaro, R. A. McLaughlin, B. R. Klyen, B. A. Wood, P. D. Robbins, C. M. Saunders, S. L. Jacques, and D. D. Sampson, "Parametric imaging of the local attenuation coefficient in human axillary lymph nodes assessed using optical coherence tomography," Biomed. Opt. Express **3**(2), 366–379 (2012).
56. R. A. McLaughlin, L. Scolaro, P. Robbins, C. Saunders, S. L. Jacques, and D. D. Sampson, "Parametric imaging of cancer with optical coherence tomography," J. Biomed. Opt. **15**(4), 046029 (2010).
57. L. X. Chin, X. J. Yang, R. A. McLaughlin, P. B. Noble, and D. D. Sampson, "*En face* parametric imaging of tissue birefringence using polarization-sensitive optical coherence tomography," J. Biomed. Opt. **18**(6), 066005 (2013).

1. Introduction

Skeletal muscle comprises multiple myofibers, which are long, columnar cells capable of contraction through the binding of the rod-like protein molecules, actin and myosin. Collections of parallel myofibers are encased within a connective sheath to form fascicles; and multiple fascicles are sheathed within a tough layer of connective tissue, the epimysium, to form an entire muscle. This connective layer is attached to tendons, and, in turn, is anchored to bone [1]. Skeletal muscle is subject to numerous fatal pathologies that compromise this structure and impair function. For example, Duchenne muscular dystrophy (DMD) is an X-chromosome linked muscle disorder that affects 1 in 3600-6000 live male births [2], caused by a defect in the gene that encodes for the structural sub-sarcolemmal protein dystrophin [3]. Pathological necrosis of myofibers leads to replacement of the muscle tissue with sclerotic tissue and fat, resulting in progressive muscle loss and eventual death [2].

#198712 - $15.00 USD Received 2 Oct 2013; revised 22 Nov 2013; accepted 30 Nov 2013; published 10 Dec 2013

Assessment of new pharmaceutical and nutritional interventions for such diseases is made difficult by a lack of techniques to assess muscle structure. Biopsy and subsequent morphological analysis of histological sections is the gold standard, but requires excision and fixation of the tissue [4]. In small animal models, such as mouse models, this will typically involve sacrificing the animal, which precludes the possibility of longitudinal study. In human studies, the use of large-gauge biopsy needles can be undesirably invasive in patients who already suffer compromised muscle function.

In vivo biomedical imaging methodologies, such as ultrasonography [5–7], magnetic resonance imaging (MRI) [8–15] or X-ray computed tomography (CT) [16–18], have been applied to muscle imaging. Ultrasonography is in both routine clinical use (for human patients) [6] and preclinical use (for animal models) [7] because of its lower cost, shorter acquisition time and avoidance of ionizing radiation. The imaging resolution, however, limits ultrasonography in resolving individual myofibers, which are typically 30 to 50 μm in diameter [4]. Although recently studies report that micro-ultrasonography [19, 20], which is applied in imaging small animals, can reach spatial resolution as fine as 30 μm [19], its capability in imaging skeletal muscle is yet to be established.

MRI has been used to provide three-dimensional (3D) imaging of dystrophic muscle not only in human patients [8, 9] but also in canine [10, 11] and murine [12–15] models. High-field strength micro-MRI has been reported to achieve a reconstructed resolution of ≈30 μm in imaging the cat visual cortex [21], but access, cost and the long acquisition times of this imaging modality still impede its uptake for resolving the microstructure of skeletal muscle.

CT has been used in both clinical assessment of muscular diseases in human patients [16], as well as in preclinical characterization and analysis of muscle in animal models with iodine contrast agents [17, 18]. Micro-CT has been also used in preclinical imaging of small animals [22]. However, the radiation exposure of CT limits its use in longitudinal human studies; and the limited bore-size of micro CT scanners precludes its extension to *in vivo* human work.

Optical imaging techniques, such as confocal [23], multi-photon [24], and second harmonic generation microscopy [25, 26], allow much higher resolution imaging of muscle structures. These techniques are able to resolve individual myofibers, but typically require *ex vivo* tissue samples. A needle probe for confocal microscopy has been developed and demonstrated to be capable of visualizing ultrastructure of skeletal muscle [27]. *In vivo* imaging of sarcomeres within mouse and human skeletal muscle tissues using optical endomicroscopy has also been reported to achieve penetration depths of a few hundred micrometers [28]. These endomicroscopic imaging modalities, however, are of limited sub 100-μm field of view.

Optical coherence tomography (OCT) [29], an interferometric technique based on the backscatter of near infrared light, provides the potential for non-destructive, high-resolution imaging of muscle structure. Previous studies have demonstrated that OCT can visualize cellular structures (e.g., individual myofibers) of skeletal muscle [30–32]. However, in common with other optical imaging methods, OCT is restricted to superficial imaging of muscle (≈2 mm).

Recent work has advanced the use of OCT needle probes for imaging deep within tissue, including in three dimensions [33–39]. In an OCT needle probe, the distal focusing optics are miniaturized and encased within a hypodermic needle [40]. The focusing optics typically comprise either a GRIN lens [33]; a ball lens [41, 42]; or a length of GRIN fiber [34, 36, 39, 43]. By redirecting the light beam perpendicular to the longitudinal axis of the needle probe and rotating the needle probe, it is possible to acquire a 2D radial scan (radial B-scan). By simultaneously inserting or retracting the needle probe, 3D imaging (C-scan) may be performed. OCT needle probes have previously been demonstrated in many tissues, including lung [35, 38], breast [37], prostate [44], and brain [45], amongst others [40].

Although minimally invasive, OCT needle probes cause some trauma to the tissue, which has driven work to minimize their diameter. This is particularly critical when imaging small animal tissues, such as those of mouse models. We have previously described a probe encased within a 30-gauge needle (30G, outer diameter of 310 μm), the smallest published side-

#198712 - $15.00 USD Received 2 Oct 2013; revised 22 Nov 2013; accepted 30 Nov 2013; published 10 Dec 2013

viewing OCT needle probe [36]. However, this preliminary design presented a number of limitations when utilized to image muscle tissue. Developed for an 840-nm OCT system, the light beam achieved only a limited image penetration depth in muscle tissue. Furthermore, losses introduced by the side-deflecting mirror coating reduced the overall system sensitivity to a level that was insufficient for imaging of tissue structures with relatively weak contrast such as muscle fibers. In addition, the manufacturing method used to chemically etch an imaging window into the shaft of the extremely thin 30G needle significantly reduced the robustness and durability of the probe.

In this paper, we address these limitations in the design and manufacture of an improved, high-sensitivity, ultrathin, side-viewing 30G OCT needle probe. We adapt the optical design to a 1300-nm OCT system, achieving an improved imaging depth. The optical losses in the mirror coating are substantially reduced, leading to a high sensitivity. We utilize laser drilling to construct an imaging window in the needle shaft, allowing more reproducible needle production without compromising the structural integrity of the needle. We present a detailed characterization of the sensitivity and beam characteristics of the probe. Using this improved OCT needle probe, we present the first published histology-matched images of muscle structure at the microscopic scale, at a depth of approximately one centimeter below the tissue surface, visualizing myofibers, tendon and connective tissue; and observing a loss of structure in areas of muscle necrosis.

2. Materials and methods

2.1 Design and fabrication of the ultrathin needle probe

The schematic of the improved ultrathin needle probe is shown in Fig. 1(a). This second-generation ultrathin OCT needle probe is designed for the 1300-nm operating wavelength band. The distal focusing optics consists of a 260-μm section of no-core fiber (NCF) and a 120-μm section of graded-index (GRIN) fiber (GIF625, Thorlabs, USA) spliced to the end of single-mode fiber (SMF-28, Corning, USA). An additional section of NCF is added after the GRIN section and polished at an angle of 45º using a fiber connector polishing machine (SpecPro 4L, Krelltech, USA). By simulating the output beam of the probe using the ABCD matrix method [46], the lengths of the NCF and GRIN fiber sections were chosen such that a full-width at half-maximum (FWHM) resolution of 20 μm or better is maintained over a depth range of several 100 micrometers in water, taking into account the astigmatism resulting from the cylindrical output window, as discussed in more detail in the following subsection.

A metal reflection coating consisting of a 3-nm chrome adhesion layer and a 300-nm gold layer is applied to the angle-polished fiber tip using a thermal vacuum deposition machine. After metallization, the fiber probe is mounted inside a 30G hypodermic needle with a 140-μm diameter side opening (as shown in Figs. 1(c) and 1(d)). In the first-generation ultrathin OCT needle probe, the side opening was fabricated via electrochemical etching using a customized setup [36]. Neither the size nor the geometry of the opening could be precisely controlled and erosion of the hypodermic needle tubing near the imaging window led to a reduction in structural integrity of the needle.

In the second-generation ultrathin OCT needle probe, the side opening was fabricated by laser ablation with a femtosecond laser micromachining system based upon a commercial Ti:Sapphire amplified femtosecond laser (Mantis (oscillator) and Legend Elite (amplifier), Coherent Inc., USA). The 800-nm, 100-fs pulsetrain with a repetition rate of 500 Hz was directed to a micromachining stage (IX-100C, JPSA, Inc. USA). The laser focal spot at the workpiece had a flat-top intensity profile and a diameter of 50 μm, and pulse energy ranged from 15 to 40 μJ. The spot was scanned in a circle of radius 45 μm, with 0.5-μm spacing between successive laser pulses. 20 to 30 passes were required to drill through the needle wall. As can be seen in the scanning electron microscope (SEM) image of the side opening in Fig. 1(c), the non-thermal ablation in the femtosecond regime eliminates problems resulting

#198712 - $15.00 USD Received 2 Oct 2013; revised 22 Nov 2013; accepted 30 Nov 2013; published 10 Dec 2013

from a heat-affected zone surrounding the hole that would otherwise compromise the structural integrity of the very thin hypodermic needle.

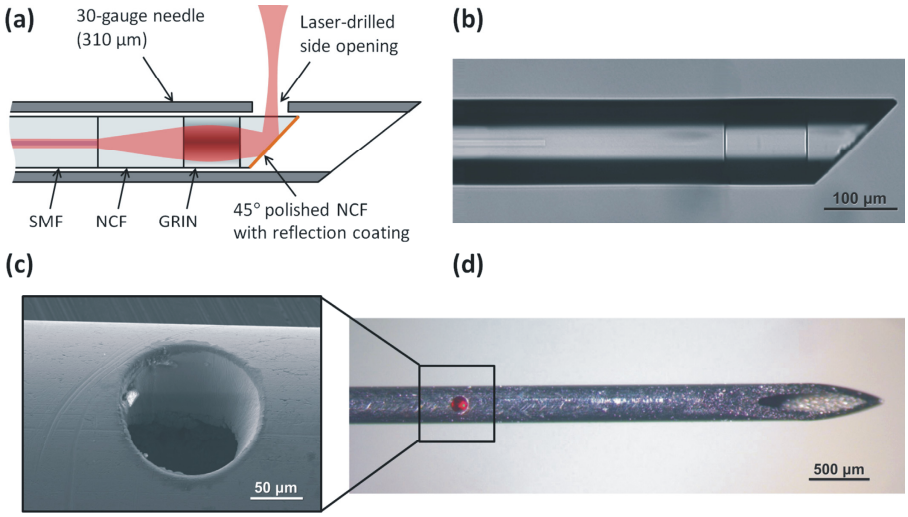

Fig. 1. (a) Schematic of the ultrathin OCT needle probe. (b) Microscope image of the angle-polished fiber probe before metallization. (c) SEM image of the laser-drilled side opening. (d) Fully assembled needle probe showing the laser-drilled side opening. In the photo, red light from the aiming laser is visible.

2.2 Optical characterization of the ultrathin needle probe

The simplicity and robustness of the side-facing ultrathin OCT needle probe design of Fig. 1(a) is obtained at the cost of some astigmatism in the output beam. The initially circular beam acquires astigmatism as it is emitted sideways from the fiber, which acts as a cylindrical lens, as illustrated in Fig. 2(a). In the *y*-direction, the beam is unaffected and comes to a focus at a working distance WD_y. In the *x*-direction, however, the beam comes to a focus at a shorter distance WD_x. In air, the high refractive-index contrast produces very strong astigmatism that renders this probe design unsuitable for use under such conditions. However, when the probe is inserted into biological tissue, it is always immersed in interstitial fluids with a refractive index similar to that of water (n = 1.321 at 1.3 µm), thereby reducing the refractive-index contrast at the silica fiber interface (n = 1.447 at 1.3 µm) to a level where the residual astigmatism of the beam is tolerable for many applications, as previously demonstrated [36].

Since a direct measurement of the beam profile in water is difficult, we used a setup that allows an indirect measurement of the output beam when the probe is immersed in water. The probe was placed in direct contact with a thin coverslip (thickness 150 µm) and immersed in a drop of water. The beam was then profiled in air behind the coverslip. This measurement procedure is valid because planar interfaces between homogenous dielectric media do not change the transverse profile of paraxial beams but simply result in a change of scale of the propagation axis [46]. The measurement was performed using a commercial near-field beam profiler that images the transverse intensity profile onto a CCD sensor using an objective lens with 12× magnification (SP620U, Ophir-Spiricon, USA). Figure 2(b) shows the FWHM beam diameters, d_x and d_y, in the x and y directions, respectively, plotted versus the distance in water from the fiber/water interface. The diameter values were obtained from fitting Gaussian profiles to the transverse intensity distributions.

The measured beam profile (solid lines in Fig. 2(b), *x*-direction in blue, *y*-direction in red) is consistent with an ABCD matrix simulation [46] of the output beam after the cylindrical fiber/water interface (dashed lines). The complex beam parameter of the output beam in the *y*-direction was obtained from a curve fit to the measured data (dashed red line in Fig. 2(b)) and, using ABCD matrix transformations, the complex beam parameters of the circular beam

#198712 - $15.00 USD Received 2 Oct 2013; revised 22 Nov 2013; accepted 30 Nov 2013; published 10 Dec 2013

within the fiber, as well as of the refracted output beam in the *x*-direction (dashed blue line in Fig. 2(b)), were calculated. The tight focus in the *x*-direction dominates the resolution and sensitivity characteristics of the probe and its location at a distance of ≈330 μm from the probe can be assumed to define the approximate working distance in water. This is also apparent when looking at the normalized on-axis intensity in Fig. 2(b) (dashed black curve), which was calculated from the measured beam diameters d_x and d_y using the relation $I_{on\text{-}axis} \propto 1/(d_x\, d_y)$ under the assumption that the beam can be well approximated by an astigmatic Gaussian beam.

The transverse intensity distribution of the elliptical spot at a distance of 330 μm from the probe is shown in Fig. 2(c), demonstrating that the probe beam has a nearly diffraction-limited Gaussian-like profile. The elliptical output beam allows imaging with a FWHM transverse resolution below 20 μm over a distance of ≈700 μm from the probe in water (or ≈740 μm in tissue with an average refractive index of n = 1.4), with peak resolutions of 8.8 μm and 16.2 μm in the *x*- and *y*-directions, respectively.

The sensitivity of the ultrathin OCT needle probe was measured in combination with a 1300-nm swept source OCT (SSOCT) scanning system (see Fig. 3) which has a theoretical shot-noise-limited sensitivity of ≈117 dB. The sensitivity of the probe was determined by measuring the signal-to-noise ratio (SNR) of the backreflection from a silica/water interface (Fresnel reflectivity of −26.8 dB). The results are displayed in Fig. 2(d), which shows an averaged (1000×) A-scan of the silica/water interface (Peak 4) positioned at the point of maximum backreflection, as well as the SNR of Peak 4 at a range of distances from the probe in water. Also visible in the A-scan are some of the internal backreflections of the probe, where Peak 1 is the splice between the GRIN fiber and the angle-polished NCF section; Peak 2 is believed to be backscattering from imperfections of the angle-polished and metalized NCF end facet; and Peak 3 is the NCF/water interface. Peak 5 is a spurious signal from the SSOCT system that is not fully suppressed by the fixed-pattern noise removal algorithm. The highest SNR is obtained at a distance of 346 μm from the probe, which is in good agreement with the beam profile measurement results of Fig. 2(b) that lead us to expect the point of maximum sensitivity to be in close vicinity of the tight focus of the *x*-direction at ≈330 μm. The peak SNR of 56.1 dB translates into a sensitivity of 108 dB, taking into account the −26.8-dB reflectivity of the silica/water interface and an additional attenuation of 25 dB, which was introduced by loosening the FC-APC connection of the sample arm fiber. The additional 25-dB attenuation was necessary to prevent saturation of the detector.

The high sensitivity of the ultrathin OCT needle probe can be attributed to its low round-trip loss of only ≈2.5 dB, which was determined by measuring the returning signal from a silver mirror aligned at the working distance under water immersion. This is a significant improvement compared to the first-generation ultrathin OCT needle probe, which had a relatively high round-trip loss of ≈10 dB, primarily caused by the absorption of the metal reflection coating in the 840-nm operating wavelength band [36]. Apart from benefiting from the lower absorption in the 1300-nm operating wavelength band, this second-generation ultrathin OCT needle probe also uses a thinner chrome adhesion layer (3-nm thickness compared to 10-nm in the first-generation needles) in order to minimize its detrimental effect on the optical properties of the gold reflection coating.

#198712 - $15.00 USD Received 2 Oct 2013; revised 22 Nov 2013; accepted 30 Nov 2013; published 10 Dec 2013

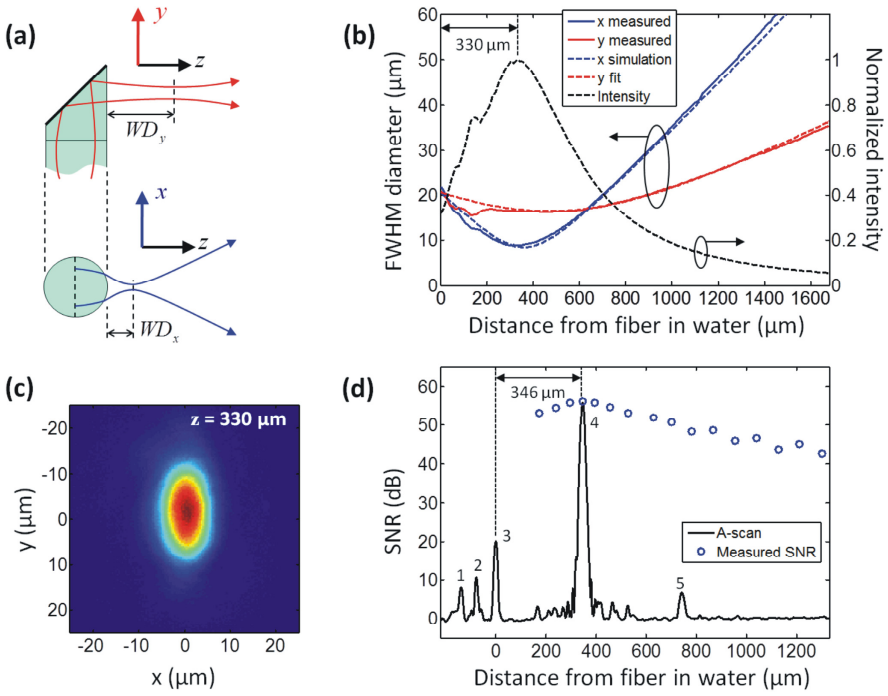

Fig. 2. Beam profile and sensitivity characterization of the probe. (a) Illustration of the astigmatism introduced by the fiber, resulting in different working distances WD_x and WD_y in the *x*- and *y*-directions. (b) Measured, simulated and fitted FWHM output beam diameters in water, and calculated normalized on-axis intensity (see text for details). (c) Transverse intensity profile of the beam in water at the focus of the *x*-direction, at a distance of 330 µm from the fiber. (d) Averaged OCT A-scan of a silica/water interface (Peak 4) located at the distance of maximum SNR. The SNR of Peak 4 over a range of distances from the probe is also shown (circles). See text for discussion of the remaining peaks.

2.3 1300-nm OCT imaging system and data acquisition

The OCT needle probe was interfaced to an SSOCT system (Fig. 3). The light source is a wavelength-swept laser (Axsun, USA) with an average power of 40 mW, a sweep rate of 50 kHz, and a full sweep bandwidth of 100 nm centered at 1310 nm. The source power is approximately constant within the sweep bandwidth, resulting in a flat-top spectral shape. For this reason, a Hann window (also known as Hanning window) is applied to the spectral data prior to the Fourier transform in order to reduce the sidelobes in the axial point spread function. The resulting FWHM axial resolution in air, after application of the Hann window, is 21 µm. The source provides a clock output that is generated using a Mach-Zehnder interferometer (MZI), allowing equidistant sampling in frequency space and eliminating the need for computationally intensive resampling of the spectral data. The 50-kHz trigger pulses from the source are gated by a synchronization signal from the needle motion controller which counter-rotates and retracts the needle during scanning. The motion controller outputs 1600 trigger pulses per 360 degree rotation of the needle, and it performs a full counter-rotation (360 degrees clockwise and anticlockwise) every second, resulting in an effective scan rate of ≈3200 A-scans per second. The OCT signal is sampled with a 12-bit, 500-MS/s digitizer card (ATS9350, Alazar Technologies, Canada).

The rotation-scanning principle employed acquires A-scans at constant angular intervals, which inherently results in a circumferential spatial sampling interval that linearly increases as a function of distance from the needle axis. For this reason, a high angular sampling density of 1600 A-scans per 360 degree rotation was chosen to ensure that, at any given distance from the needle, the circumferential sampling is always finer than the FWHM

#198712 - $15.00 USD Received 2 Oct 2013; revised 22 Nov 2013; accepted 30 Nov 2013; published 10 Dec 2013

transverse resolution of the beam (see Fig. 2(b)). For example, at the maximum expected useful imaging depth in scattering tissue of ≈2 mm, the circumferential sampling interval has a size of ≈8 μm, which is smaller than the transverse resolution at that depth.

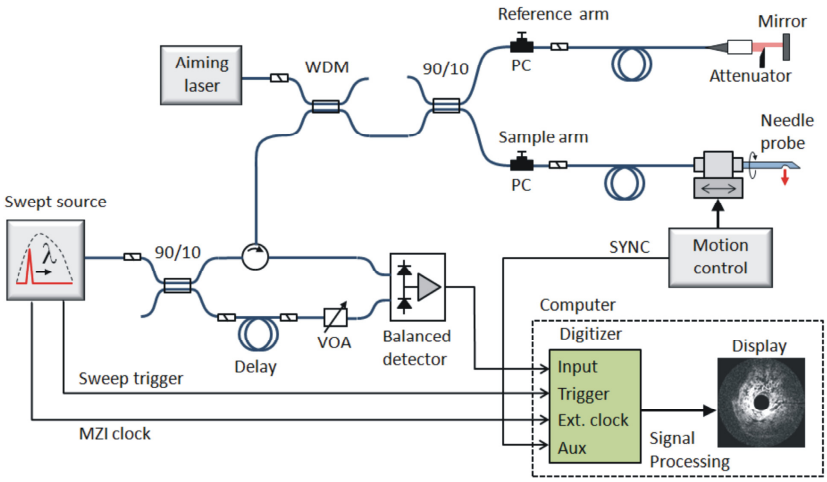

Fig. 3. Schematic of the 1300-nm SSOCT needle imaging system. MZI, Mach-Zehnder interferometer; WDM, wavelength-division multiplexer; VOA, variable optical attenuator; SYNC, synchronization signal; PC, polarization controller.

2.4 Skeletal muscle imaging experiments

All the animal work conformed to the guidelines of the National Health & Medical Research Council (Australia) Code of Practice for the Care and Use of Animals for Scientific Purposes (2004) and the Animal Welfare Act of Western Australia (2002), and was approved by the University of Western Australia Animal Ethics Committee. To demonstrate the ability of the needle probe to image the structure of skeletal muscle, normal and dystrophic mouse skeletal muscle samples, from either forelimbs or hindlimbs, were excised as intact muscles by an experienced physiologist. Immediately after excision, the samples were stored at room temperature in phosphate-buffered saline. Imaging experiments were carried out within six hours of sample collection. We imaged five normal mouse muscles and five dystrophic mouse muscles (in each case two triceps, two quadriceps, and one tibialis anterior muscle). The ultrathin OCT needle probe was inserted ≈10 mm deep at one location on each muscle sample. This location was marked by a piece of surgical thread penetrating the muscle sample perpendicularly to the needle tract to aid in its identification in subsequent histology. OCT C-scans were acquired as the needle probe was counter-rotated at 1 Hz and retracted over a distance of 4 – 6 mm at a speed of 5 μm/s in discrete steps of 5 μm.

After scanning, the intact muscle samples were immediately fixed in formalin solution. The samples were embedded in paraffin and sectioned into 5 μm-thick sections at 90-μm intervals in accordance with standard histological procedures. Using the surgical thread as the indicator of the imaged area, these sections were taken parallel to the needle trajectory. Sections were stained with haematoxylin and eosin (H&E) and digitally photo-micrographed (Scanscope, XT, Aperio Technologies Inc., Vista, California, USA). The 3D OCT data volumes were visualized using in-house visualization software (OCTView) and oblique views were visualized to match the histological sections by correlating multiple structural features over a range of depths of both the 3D-OCT volumetric data set and H&E-stained histological sections.

#198712 - $15.00 USD Received 2 Oct 2013; revised 22 Nov 2013; accepted 30 Nov 2013; published 10 Dec 2013

3. Results

Figure 4 shows a 2D OCT image extracted from a 3D data volume acquired on a mouse quadriceps muscle, and the matching H&E histology. To obtain corresponding images, an oblique longitudinal image was extracted from the 3D OCT data volume and orientated so as to be parallel and adjacent to the needle probe, thus, the needle shaft is not visible. In this oblique OCT image slice, each horizontal row of the image intersects a different radial B-scan. The reduced signal strength (darker tones) on the left and right of the image correspond to areas of muscle tissue that are the most distant from the needle probe. Myofibers (see examples labeled by arrowheads and MF) in the OCT image appear as a characteristic striated pattern, with the boundary of the fascicle marked by highly backscattering connective tissue (labeled C) or tendon (labeled T). Good correspondence is observed in the orientation of the myofibers between the OCT needle images in fresh tissue and the matching fixed histological section.

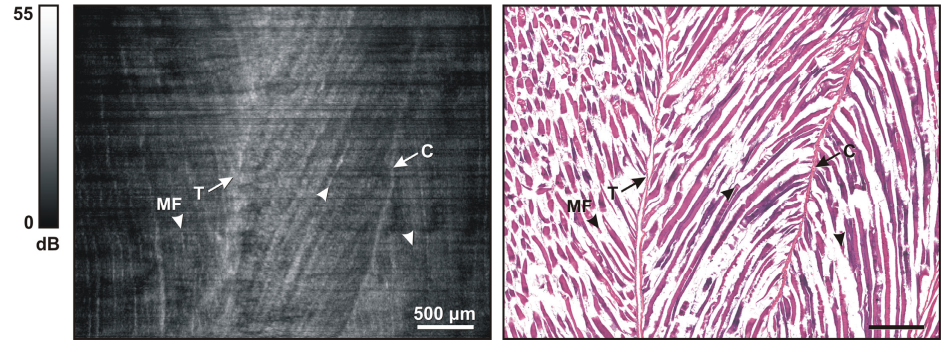

Fig. 4. Representative images of normal mouse skeletal muscle. (Left) OCT oblique slice taken from the 3D OCT volumetric data set. The striated appearance indicates the highly organized arrangement of the myofibers (MF and/or arrowhead). Several structures with higher signal intensity indicate tendon (T) and connective tissue (C). (Right) Corresponding H&E histology.

Figure 5 shows representative images obtained from a dystrophic muscle sample taken from the quadriceps muscle of an *mdx* mouse [4]. As with Fig. 4, a longitudinal image was extracted from the 3D OCT volume and matched against histology. The characteristic striated pattern of myofibers can be seen in the left most area of the image (see examples labeled by arrowheads and MF), correlating with myofibers visible in the matching histology. An area of necrosis is visible in the middle section of the histology image, marked by the appearance of purple-stained, basophilic inflammatory cells, and a "broken" appearance in the adjacent myofibers. This presents in the OCT image as a loss of striated texture of myofibers (labeled Necrosis). The normal and necrotic regions are clearly delineated by connective tissue (labeled C), visible in both images. The appearance of both healthy and necrotic regions of skeletal muscle imaged with the OCT needle probe are consistent with earlier results obtained with a standard, external-scanning benchtop OCT system [30, 31]. The OCT image, however, does not show a structure corresponding to the connective tissue in the right-hand-side of the histological slide. This is probably because of insufficient signal intensity within that corresponding region in the OCT image.

Several views of a 3D rendered visualization of the mouse skeletal muscle OCT image are shown in Fig. 6, and the associated video is available as Media 1. During each scan, a 3D cylinder of OCT data is acquired, with the central axis located along the needle trajectory (labeled N), and the radius of the cylinder corresponding to the image depth from the needle shaft. Figure 6(a) shows the uncropped data set, with the dashed lines indicating the different cropping planes used in Fig. 6(b)-6(d). Note that Fig. 6(d) is cropped to show the imaging plane that was histology matched in Fig. 4. Cropping of the 3D data allows inspection of the 3D structure of the muscle fibers. Connective tissue and tendon are also visible, labeled C and T, respectively, from different orientations.

#198712 - $15.00 USD Received 2 Oct 2013; revised 22 Nov 2013; accepted 30 Nov 2013; published 10 Dec 2013

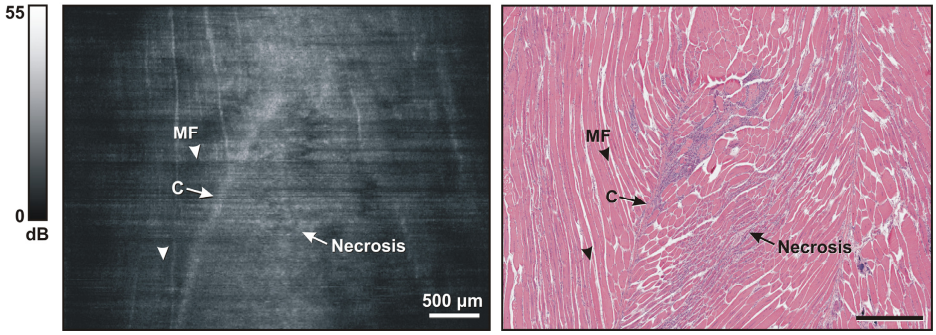

Fig. 5. Representative images of dystrophic mouse skeletal muscle. (Left) OCT oblique slice taken from the 3D OCT volumetric data set. The striated appearance indicates the highly organized arrangement of myofibers (MF and/or arrowhead). The structure with higher intensity indicates connective tissue (C). Muscle necrosis is visible as a region without striated appearance (Necrosis). (Right) Corresponding H&E histology.

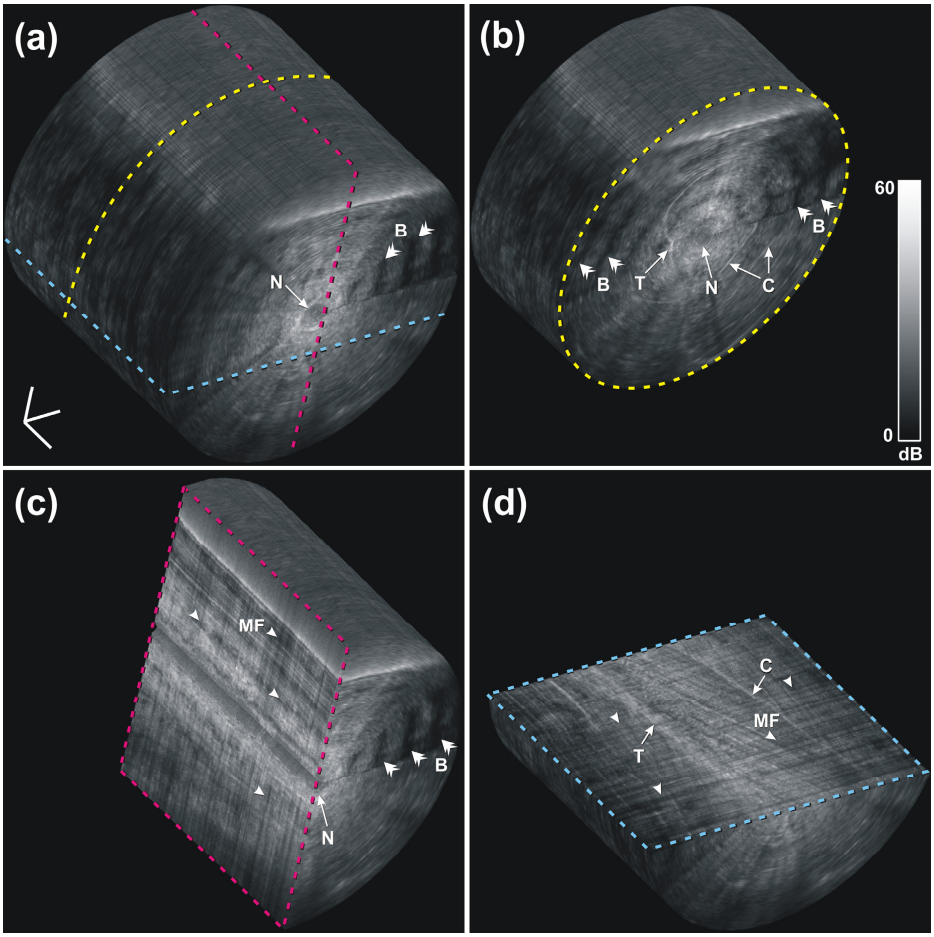

Fig. 6. A 3D-rendered volumetric OCT data set of normal mouse muscle at an approximate depth of 10 mm in a) and three orthogonal cross sections in b), c) and d). The cross section in d) shows the same image plane as that of Fig. 4, but the brightness and contrast in the visualization software were adjusted differently in this 3D view to enhance the appearance of the full data set, yielding a slightly different dynamic range on the color bar compared to Fig. 4. B, birefringence artifacts; C, connective tissue; MF, myofibers; N, needle tract; T, tendon. The 3D scale bar in a) represents 500 µm in each direction (Media 1).

#198712 - $15.00 USD Received 2 Oct 2013; revised 22 Nov 2013; accepted 30 Nov 2013; published 10 Dec 2013

Healthy skeletal muscle tissue is highly birefringent, arising from the highly organized anisotropic cellular structure and arrangement of myofibers [47–49]. This results in a banding pattern in the OCT image. The banding pattern is visible in the 3D visualization (see examples labeled by double arrow heads and B). It has been demonstrated that polarization-sensitive OCT (PS-OCT) is able to differentiate exercised dystrophic mouse muscle from healthy muscle by detecting their different levels of birefringence [50]. In separate research, we have shown that quantitative analysis of birefringence in a PS-OCT scan may be used to automatically identify areas of necrosis in skeletal muscle tissue [51].

4. Discussion

The images presented here demonstrate the potential of OCT needle probes to visualize the microstructure of mouse skeletal muscle at a depth of approximately one centimeter below the tissue surface, and discern differences between tissue types. Regions of healthy mouse muscle presented with a characteristic striated appearance, consistent with the alignment of the individual myofibers. This was shown to be different for an area of necrosis, wherein the destruction of the myofibers gave rise to areas of non-textured, more homogeneous backscatter. Regions of mouse muscle tissue were well delineated by the higher backscatter of tendon and connective tissue.

While earlier studies have demonstrated the ability of OCT to image mouse skeletal muscle tissue [30–32], the shallow image penetration depth restricts the utility of such methods. Deployment through a needle probe represents a significant step forward in the utility of OCT, providing one solution to address the limited image penetration depth. Assessment of larger areas of muscle tissue, involving multiple acquisitions, would provide a sampling of tissue integrity throughout the muscle. An open question remains as to the number of such acquisitions required to provide a statistically robust characterization of structure within a larger muscle. This number will depend upon the pathology, with more homogeneous pathologies likely to be sufficiently characterized by more sparsely distributed imaging acquisitions. Optimal needle placement may also be guided by a complementary imaging modality such as ultrasound, as demonstrated in [52].

The ultrathin OCT needle probe described in this paper has several technical improvements over our earlier design [36], leading to the good image quality reported here. The sensitivity gain was achieved by adapting the design for operation at 1300 nm in combination with an SSOCT system with substantially higher baseline sensitivity than the previously used 840-nm SDOCT system, and by reducing the optical losses of the probe through improvements in the fabrication process. Operation at 1300 nm, furthermore, was observed to improve the image penetration depth due to the reduced scattering at longer wavelengths [53, 54]. In addition, improved mechanical robustness was obtained by using non-thermal ablation with femtosecond laser pulses to fashion the imaging window. This also provided improved control over the dimensions of the window and improved structural integrity of the adjacent sections of the needle shaft. Such improvements in the OCT needle manufacturing process are important steps to transition these probes from an optics research environment to the larger-scale production required for pre-clinical and clinical usage.

The 2D OCT images of Figs. 4 and 5 exhibit some horizontal striations (perpendicular to the needle axis), caused by variation in the SNR of individual B-scans. We observed this to be due to small, isolated pieces of tissue being temporarily lodged in the needle hole through which imaging occurs. Such tissue debris is typically cleared within one or two rotations of the needle probe. The effects of such tissue debris could be reduced by increasing the spatial sampling density in the pullback direction and performing spatial averaging along that axis in post-processing.

The utility of OCT needle probes in the diagnostic assessment of muscle pathology could be enhanced by employing quantitative image analysis for identifying regions of diseased tissue. We note that a range of such techniques is under development, quantifying the distinction between diseased and healthy tissue using optical properties such as the optical attenuation coefficient [55, 56] or birefringence [51, 57].

#198712 - $15.00 USD Received 2 Oct 2013; revised 22 Nov 2013; accepted 30 Nov 2013; published 10 Dec 2013

5. Conclusion

In this paper, a highly optimized, high-sensitivity, ultrathin, side-viewing OCT needle probe has been presented. With an outer diameter of 310 μm, the needle probe presents a minimally invasive means of performing OCT imaging deep within tissue. We have presented the first published 3D OCT data volumes of mouse skeletal muscle obtained by an OCT needle probe of significantly improved performance and validated against co-registered H&E histology sections. Results demonstrated the ability of such needle probes to distinguish the appearance of healthy and necrotic mouse muscle tissue, and differentiate such areas from connective tissue and tendon. These preliminary findings demonstrate the potential of OCT needle probes to provide a new way to visualize *in situ*, deep within the tissue, the structure and integrity of skeletal muscle.

Acknowledgments

The authors acknowledge Dr. Gavin J. Pinniger for providing the skeletal muscle tissue samples. The authors acknowledge the facilities, and the scientific and technical assistance of the Australian Microscopy & Microanalysis Research Facility at the Centre for Microscopy, Characterisation and Analysis, The University of Western Australia, a facility funded by the University, State and Commonwealth Governments. We also wish to acknowledge CELLCentral, University of Western Australia, for the preparation of histological slides. We acknowledge the support from the Western Australian node of the Australian National Fabrication Facility for vacuum deposition of the metal reflection coatings in the OCT needle fabrication, and we especially thank Nir Zvison. We also thank Peijun Gong for his help in the generation of the video. Robert A. McLaughlin is supported by a fellowship from Cancer Council Western Australia and this research is supported in part by funding from the National Breast Cancer Foundation, Australia.